Journal of Magnetism and Magnetic Materials 552 (2022) 169212

Contents lists available at ScienceDirect

Journal of Magnetism and Magnetic Materials

journal homepage: www.elsevier.com/locate/jmmm

The supporting capacity of ferrofluids bearing: From the liquid ring to droplet

Hao Xu, Qingwen Dai, Wei Huang *, Xiaolei Wang

National Key Laboratory of Science and Technology on Helicopter Transmission, Nanjing University of Aeronautics & Astronautics, Nanjing 210016, China

ARTICLE INFO

Keywords:
Ferrofluids bearing
Supporting force
Magnetic field intensity

ABSTRACT

In this paper, a simple ferrofluids (FFs) bearing, which consists of a rotor, a stator embedded with a cylinder magnet, and FFs is proposed. By controlling the volume of FFs, two types of liquid structures of the ring and droplet shapes are formed on the stator surface. Models of the bearing for the static supporting force are established and validated by experiments. The multicycle loading-unloading of the FFs bearings as well as the dynamic supporting force are performed. Results show that the static supporting force of the bearings can be predicted approximately by the theoretical model. Multicycle loading-unloading tests indicate that force values with excellent repeated accuracy can be achieved only within a limited range of oscillation in gap height. Compared with the FFs droplet bearing, the rotation speed manifests more significant impact on the dynamic supporting force of the ring structured bearing. Such design presents a new thought for micro-electro-mechanical system (MEMS) that requires precision supporting or frictionless bearing.

1. Introduction

To minimize the friction and wear in macroscale, fluid lubricated films are often used to avoid direct solid-solid contact. Two successful examples are the hydrodynamic and hydrostatic bearings due to the load carrying capacity of the pressurized lubricants. With the miniaturization of mechanical and electronic devices, the surface force plays a more important role[1]. Combining with the high surface-to-volume ratio, it is imperative to deal with adhesion, friction, and wear in the contact surfaces[2]. The traditional bearings with pressurized fluid are not as universally applicable.

Recently, liquid bridge bearings have provided a new way to produce liquid carrying capacity[3–7]. Surface tension between the liquid film and the alternant hydrophilic/hydrophobic surfaces plays as the load bearing mechanism[8]. Restrained by the energy barrier of the hydrophilic/hydrophobic border, the liquid maintains on the hydrophilic surface[3]. When compressed, the Laplace pressure formed in the liquid can offer a carrying capacity. This method has provided a successful thought to the design of MEMS rotary motors. However, the fabrication process of the hydrophilic/hydrophobic surface is complicated and the load carrying capacity of the liquid bridge bearing is relatively low, usually in the order of 10^{-1}N[6]. Questions then arise: besides the energy barrier at the hydrophilic/hydrophobic surface boundary, is there any other way to anchor the liquid? Furthermore, can the bearing capacity be further increased?

Ferrofluids (FFs) are stable colloidal suspensions of magnetic particles dispersed in a carrier liquid[9]. The typical diameter of the particles is about 10–15 nm[10]. Thermal energy maintains the particles from settling in the gravitational field and a suitable organic surfactant is decorated on the surface of each particle to prevent coagulation due to magnetic dipole interaction and van der Waals force[11].

One of the interesting and important features of FFs is that they can be controlled and positioned in a target region by an external magnetic field[12]. More importantly, the external magnetic field may produce attractive forces on each particle, which may transform to a controllable magnetostatic force in the FFs[13]. From the mechanical point of view, such kind of magnetostatic force in the fluid may just supply a bearing capacity or undertaken a normal load.

Fig. 1a shows a cylinder magnet (Φ12 mm × 2 mm) embedded into a ring 3D-print resin (Φ60 mm × Φ12 mm × 2 mm). The surfaces of the magnet and resin are in the same plane. When dropping a volume of 150 μL FFs, a liquid ring forms on the edge of the magnet (see in Fig. 1b). While the volume of the fluid increases to 600 μL, a droplet appears. Obviously, either the liquid ring or droplet can both bear a normal load. For the droplet, the bearing force merely comes from the magnetostatic force of the magnetized FFs. However, for the liquid ring structure, not

* Corresponding author.at: Yudao street 29#, Nanjing China.
E-mail address: huangwei@nuaa.edu.cn (W. Huang).

https://doi.org/10.1016/j.jmmm.2022.169212
Received 16 December 2021; Received in revised form 13 February 2022; Accepted 21 February 2022
Available online 22 February 2022

only the FFs, but the air sealed by the FFs rings will generate the carrying capacity together. Then, how the volume of FFs affects the bearing capacity? And what is the corresponding physical mechanism? There is little knowledge about it.

In this paper, two simplified models of the liquid bearing structure are established and their carrying capacities are calculated theoretically. Meanwhile, experiments are carried out and the measured results are compared with the calculated bearing forces. In addition, the multicycle loading-unloading test as well as the dynamic bearing force of the two liquid structures are also discussed.

2. Principle analysis

Fig. 2a presents the sketch map of the FFs ring bearing. When compressed, the magnetized FFs and the air sealed in the ring chamber can both produce the supporting force. Fig. 2b shows the geometrical model of a cross-sectional view of the FFs ring between two plates. Assuming that the FFs is an incompressible fluid, based on the Bernoulli equation, the pressure difference (Δp_m) between the magnetic pressure (p_i) (i is the point of the upper contact interface) and the atmospheric pressure (p_o) can be written as[14]

$$\Delta p_m = p_i - p_o = \mu_o \int_{H_{r_{out}}}^{H_{r_i}} M(H)dH \tag{1}$$

where μ_o is the magnetic permeability of the vacuum, M is the magnetization of FFs and H is the magnetic field intensity at the corresponding position.

For an ideal dilute FFs with spherical magnetic particles, the magnetization (M) of the fluid can be described by Langevin equation [15]

$$L(\xi) = \frac{M}{M_s} = \coth\xi - \frac{1}{\xi} = \frac{e^{2\xi}+1}{e^{2\xi}-1} - \frac{1}{\xi} \tag{2}$$

where M_s is the saturation magnetization of the FFs, ξ is the Langevin parameter, which can be written as

$$\xi = \frac{\mu_o m_d H}{kT} = \alpha H(\alpha = C) \tag{3}$$

where m_d is the magnetic dipole moment of the particle, k is the Boltzmann's constant and T is the absolute temperature. For the spheric magnetic particles, m_d is given as[15]

$$m_d = \frac{1}{6} M_d \pi d^3 \tag{4}$$

where d is the diameter of the particle and M_d is the domain magnetization. The saturation magnetization and the domain magnetization are related by

$$M_d = M_s / \varnothing_d \tag{5}$$

where $\varnothing_d$ is the volume fraction of the particle in the fluid.

As can be seen, the magnetization of FFs (M) is a function of the external magnetic field intensity (H). The magnetic field distribution above the magnet at different heights can be obtained by the finite element analysis. Thus, the corresponding ratio of M/M_s of FFs can also be calculated and shown in Fig. 3.

When considering the magnetic field intensity on the magnetization of the FFs, the Eq.(1) can be rewritten as

$$\Delta p_m = \mu_0 \int_{H_{r_{out}}}^{H_{r_i}} M(H)dH = \mu_0 M_s \frac{1}{\alpha}\left[ln\frac{e^{2\alpha H_{r_i}}-1}{H_{r_i}e^{\alpha H_{r_i}}} - ln\frac{e^{2\alpha H_{r_{out}}}-1}{H_{r_{out}}e^{\alpha H_{r_{out}}}}\right] \tag{6}$$

Thus, at a certain gap height, the supporting force of the liquid ring can be calculated by integrating the Δp_m from the r_{in} to r_{out}. Therefore, the force (F_{Mag}) only generated by the magnetized liquid ring can be written as

$$F_{Mag} = 2\pi r \mu_o M_s \int_{r_{in}}^{r_{out}} \left[\frac{1}{\alpha}\left(\ln\frac{e^{2\alpha H_{r_i}}-1}{H_{r_i}e^{\alpha H_{r_i}}} - \ln\frac{e^{2\alpha H_{r_{out}}}-1}{H_{r_{out}}e^{\alpha H_{r_{out}}}}\right)\right] dr \tag{7}$$

The next work is to determine the positions of the r_{in} and r_{out}. For the FFs ring structure (see in Fig. 2b), the internal and external air/fluid interfaces depend on the space isomagnetic line of the magnet. When the upper plane is at a certain gap height, the internal air/fluid interface of the fluid should locate at the position of the highest magnetic field intensity ($H_{r_{in}}$). Then, the position of r_{in} can be determined according to distribution of the field intensity along radial direction of the magnet. Fig. 4 presents an example and it gives the magnetic field distribution at the gap height of 0.4 mm. The radial position, where the highest magnetic field intensity locates is about 5.85 mm. Thus, the r_{in} = 5.85 mm.

As shown in Fig. 2b, based on the size of r_{in}, the volume (V_{air}) of the air chamber sealed by the FFs ring can be approximately calculated by the Eq.(8)

$$V_{air} = \pi(r_{in} - \frac{\Delta L_{in}}{2})^2 h = \pi(r_{in} - \frac{r_{1_{in}}\cos(90^\circ - \theta_{inB})}{2})^2 h \tag{8}$$

where $r_{1_{in}}$ is the curvature radius of the internal interface of the FFs ring and it can be obtained from the following equation:

$$r_{1_{in}} = \frac{h}{1 - \sin(90^\circ - \theta_{inB})} \tag{9}$$

where h is gap height and θ_{inB} is the angle between the tangent of the internal interface isomagnetic line and the horizontal line.

For the position of the external point r_{out}, it can be expressed as

$$r_{out} = \sqrt{\frac{V_{af}}{\pi \bullet h}} - \Delta L_{out} \tag{10}$$

where $V_{af} = V_{air} + V_f$ is the total volume of the gas (V_{air}) and FFs (V_f).

As shown in Fig. 2b, ΔL_{out} can be calculated approximatively by the following equation

$$\Delta L_{out} = r_{1_{out}}(\sin(180^\circ - \theta_{outB}) - \sin(180^\circ - \theta_{outA})) \tag{11}$$

where θ_{outA} and θ_{outB} are the angles between the tangent of the external interface isomagnetic line and the horizontal line. $r_{1_{out}}$ is curvature radius of the external air/fluid interface, which can be calculated as follow

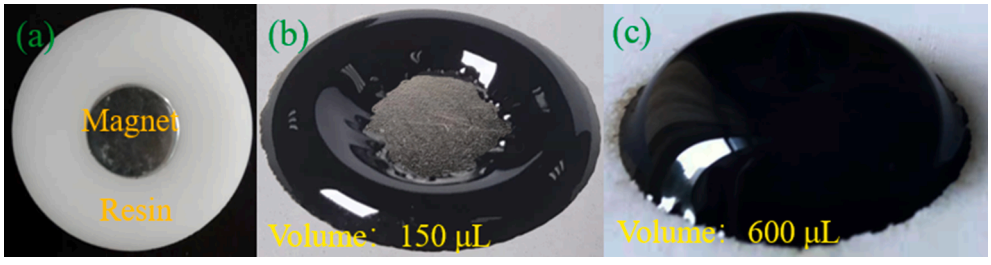

Fig. 1. (a) A ring 3D-print resin embedded with a cylinder magnet; (b) and (c) the appearances of the sample covered with 150 μL and 600 μL of FFs, respectively.

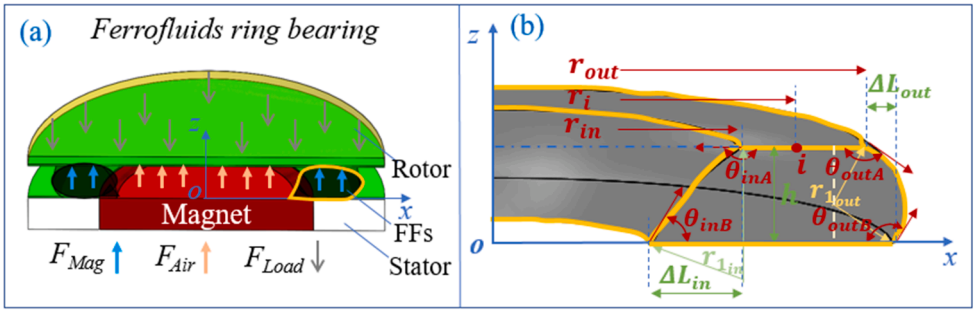

Fig. 2. (a) Sketch map of the FFs ring bearing; (b) Geometrical model of a cross-sectional view of the FFs ring between two plates.

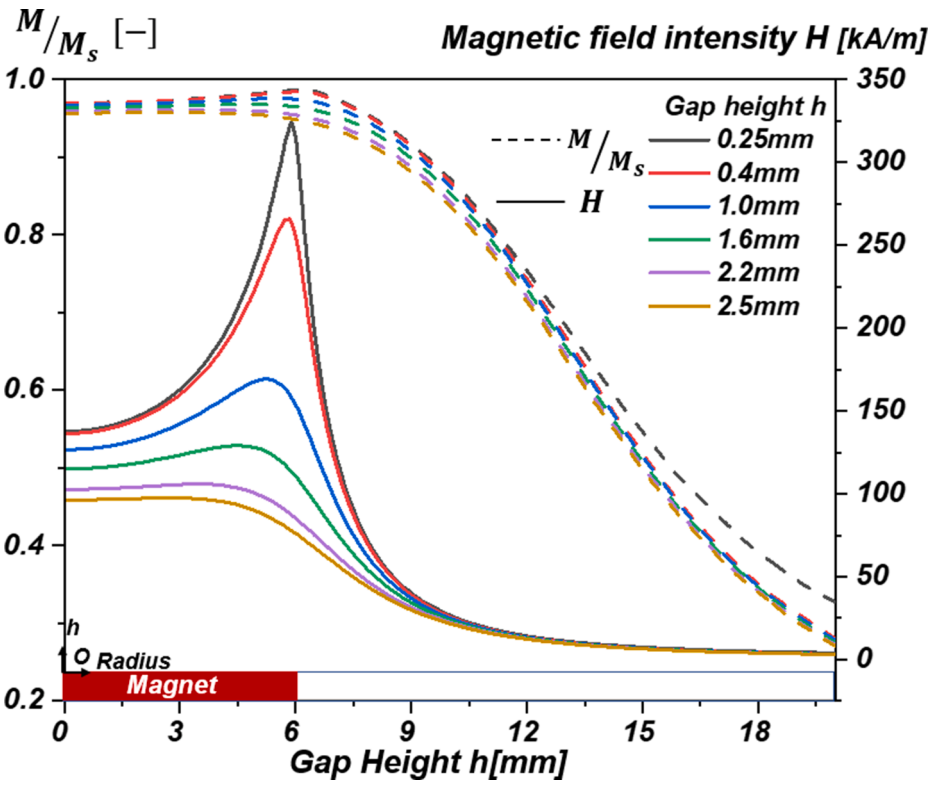

Fig. 3. Magnetic field distribution and corresponding ratio of M/M_s above the magnet at different gap height.

$$r_{1_{out}} = \frac{h}{\cos(180^\circ - \theta_{outA}) + \cos(180^\circ - \theta_{outB})} \tag{12}$$

Since the positions of the r_{in} and r_{out} are determined, the supporting force produced by the FFs ring (F_{Mag}) can be calculated by Eq.(7).

The load capability of the air chamber (F_{Air}) can be regarded as the pressure difference between the internal and external interfaces acting on the bearing surface with an area of $\pi {r_{in}}^2$. Therefore, it can be calculated as

$$F_{Air} = \Delta p_m \bullet \pi {r_{in}}^2 = \mu_o M_s \frac{1}{\alpha}\left(\ln\frac{e^{2\alpha H_{r_{in}}} - 1}{H_{r_{in}} e^{\alpha H_{r_{in}}}} - \ln\frac{e^{2\alpha H_{r_{out}}} - 1}{H_{r_{out}} e^{\alpha H_{r_{out}}}}\right) \bullet \pi {r_{in}}^2 \tag{13}$$

Eventually, the total bearing force (F_{Total}) produced by the FFs ring structure at a certain gap height can be written as

$$F_{Total} = F_{Mag} + F_{Air} = 2\pi r \mu_o M_s \int_{r_{in}}^{r_{out}} \left[\frac{1}{\alpha}\left(\ln\frac{e^{2\alpha H_{r_i}} - 1}{H_{r_i} e^{\alpha H_{r_i}}} - \ln\frac{e^{2\alpha H_{r_{out}}} - 1}{H_{r_{out}} e^{\alpha H_{r_{out}}}}\right)\right] dr$$

$$+ \mu_o M_s \frac{1}{\alpha}\left(\ln\frac{e^{2\alpha H_{r_{in}}} - 1}{H_{r_{in}} e^{\alpha H_{r_{in}}}} - \ln\frac{e^{2\alpha H_{r_{out}}} - 1}{H_{r_{out}} e^{\alpha H_{r_{out}}}}\right) \bullet \pi {r_{in}}^2 \tag{14}$$

Fig. 5a presents the sketch map of the FFs droplet bearing. When compressing, the total supporting force (F_{Total}) is supplied approximately by the magnetostatic force (F_{Mag}) of the fluid. Based on the Eq.(7), it can be written as

$$F_{Total} = F_{Mag} = 2\pi r \mu_o M_s \int_0^{r_{out}} \left[\frac{1}{\alpha}\left(ln\frac{e^{2\alpha H_{r_i}} - 1}{H_{r_i} e^{\alpha H_{r_i}}} - ln\frac{e^{2\alpha H_{r_{out}}} - 1}{H_{r_{out}} e^{\alpha H_{r_{out}}}}\right)\right] dr \tag{15}$$

Here, the shape of the FFs is a droplet. Compared with the FFs ring bearing, r_{in} in this FFs droplet model should be located at the origin of the z-axis. It means $r_{in} = 0$. Referenced by Eq.(10), Eq.(11) and Eq.(12), r_{out} can be obtained easily.

3. Experimental section

The main structure of FFs bearing consists of a rotor, FFs and a stator, as shown in Fig. 2a. The material of the rotor is a circular glass plate with the size of Φ60 × 0.5 mm. Fig. 1a presents the image of the stator, which is a ring 3D-print resin (Φ60 × Φ12 × 2 mm) embedded with a cylinder magnet (N35 NdFeB, Φ12 × 2 mm). A water-based FFs is used and its main properties are shown in Table.1. To weaken the adhesion effect,

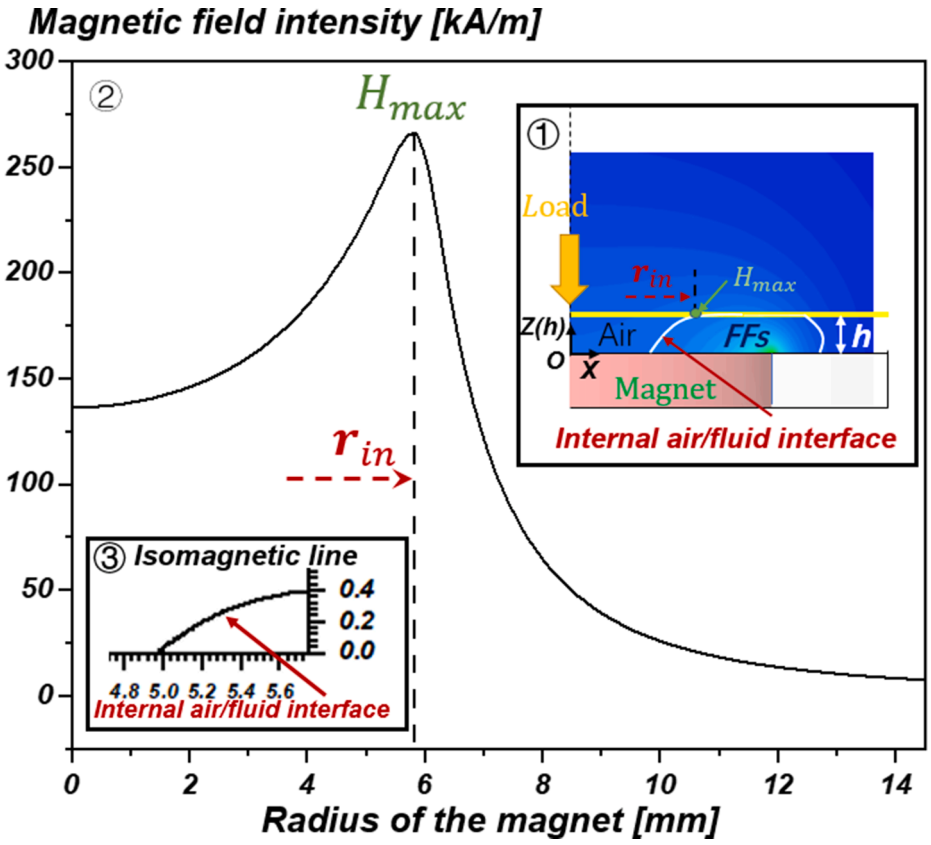

Fig. 4. The magnetic field distribution at the gap height of 0.4 mm.

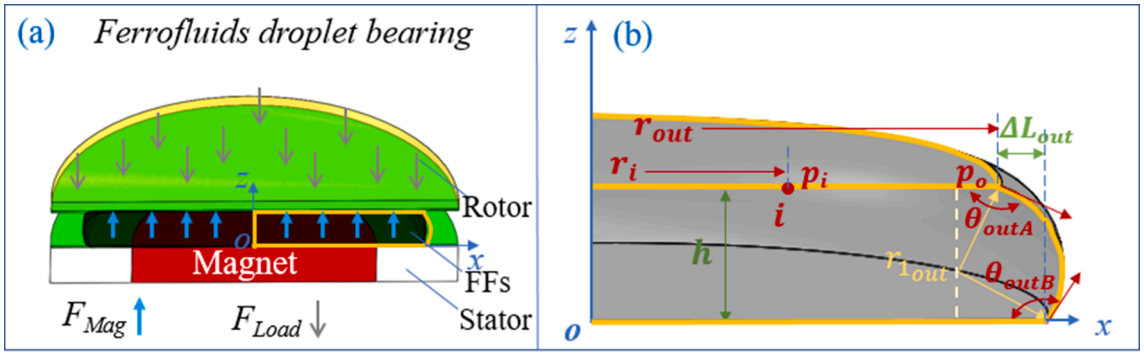

Fig. 5. (a) Sketch map of the FFs droplet bearing; (b) Geometrical model of a cross-sectional view of the FFs droplet between two plates.

Table 1
Main properties of the FFs.

Parameters	*Values*
d: Particle diameter	10 ±5nm
ρ: Density	1.18 g/cm^3
γ : Surface tension	2.6 × 10^{-4}N/cm
M_d: The domain of magnetization	450 kA/m
M_s: Saturation magnetization	23.9 kA/m
$\varnothing_p$: Volume fraction of particles	5.3%

the lower surface of the rotor and the resin surface of the stator are coated with a super hydrophobic coating (Never Wet, Ross Technology Crop. USA).

The supporting force of the FFs bearings is measured by using a stress testing platform. The rotor, which is connected with a dynamometer (Shandu SH-5) shifts in the axial direction at the speed of 0.008 mm/s. The resolution and range of the dynamometer are 0.001 N and 5 N, respectively. The supporting force of the bearing is recorded by an NI data acquisition card as the rotor moves down gradually. The static bearing capacity is defined as the rotor moves without rotation. Correspondingly, the dynamic force is defined as the rotor shifting with different rotational speeds. To examine the repeatability of the force, the rotor is carried out by a multiple loading-unloading experiment.

4. Results and discussion

Fig. 6 shows the experimental results of the static supporting force of the bearing against the gap height (*h*) with different volumes of the FFs. As the rotor moves down, the supporting force increases gradually. Due to the various volumes of the fluid, the forces are detected at different original gap heights. It can be found that, with the increasing of the FFs volume, the appearances of the liquid change from the ring structures to the shape of droplet. For the stator covered with 150 μL FFs, the

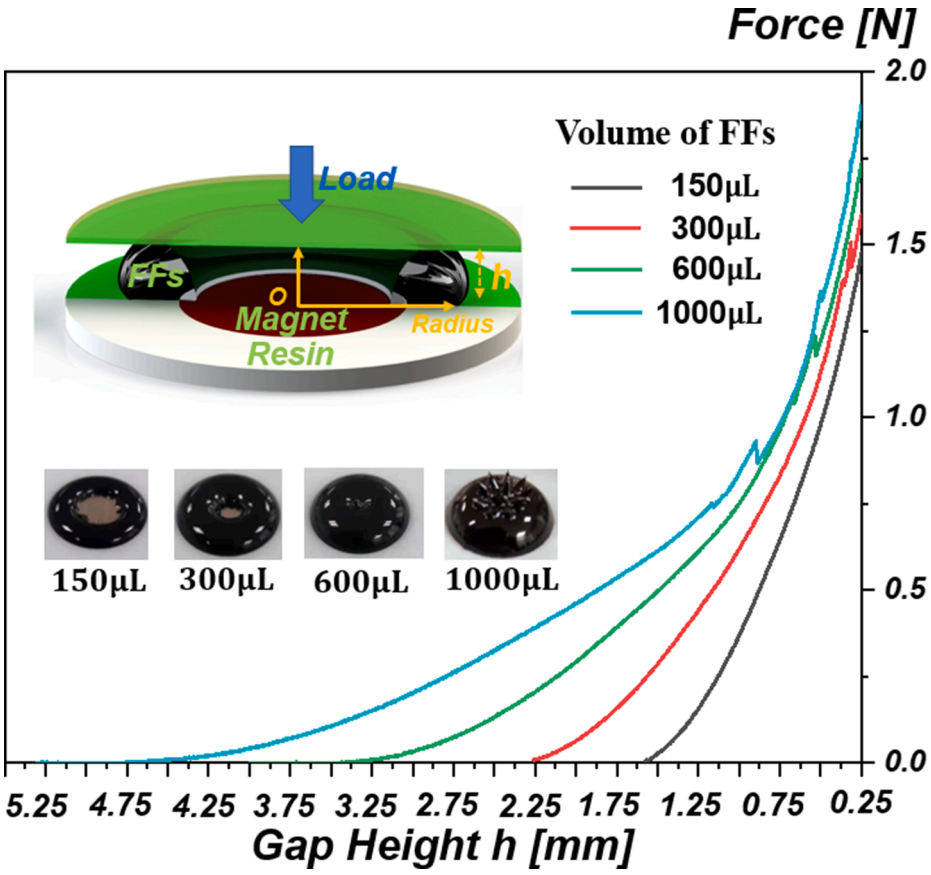

Fig. 6. Effects of the FFs volume on the static supporting force of the bearings.

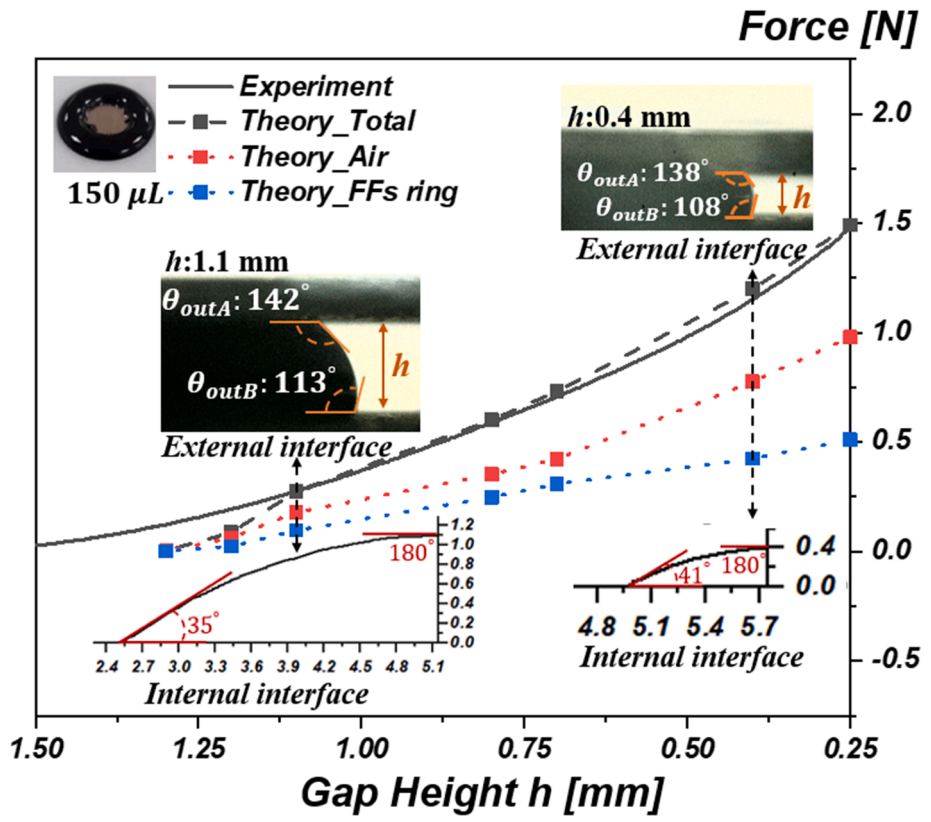

Fig. 7. Comparison of theoretical and experimental values of the static supporting force of the FFs ring bearing.

maximum supporting force is about 1.476 N at the gap height of 0.25 mm. The force increases to 1.901 N when using 1000 μL FFs. Generally, the carrying capacity of the bearing enhances with the increment of the FFs volume.

However, as the volume of FFs is higher than 300 μL, a small liquid droplet will overflow from the stator surface due to the decreased gap height and the force presents a sudden drop. The larger volume of the FFs is, the earlier force drop appears. As the rotor continue moving down, the force generated by the remaining FFs increases continuously. When another small FFs droplet escapes, the force drops again.

Fig. 7 shows the theoretical and experimental values of the static supporting force of the FFs ring bearing. The volume of the FFs is controlled at 150 μL. Based on the theoretical model (shown in Fig. 2), the supporting forces of the FFs ring (F_{Mag}, blue dot line) and the sealed air in the ring chamber (F_{Air}, red dot line) were both calculated. And the total theoretical value (F_{Total}, black dot line) is the sum of the FFs ring and the sealed air together. As can be seen, among the total force, the contribution of the sealed gas is higher than that of the FFs ring. And the difference is more distinct in the lower gap height. Generally, the experimental and theoretical values both increase with the decreasing of the gap height, showing the similar tendency.

Here is an example of the numerical procedure at the gap height of 0.4 mm (see in Fig. 7). As shown in Fig. 2b, the internal radius of the FFs interfacer_{in} = 5.85 mm, which can be obtained based on the position of the highest magnetic field intensity ($H_{r_{in}}$ = 265.95 kA/m, see in Fig. 4) at the gap height of 0.4 mm. The outline of the internal interface of the FFs depends on the isomagnetic line of $H_{r_{in}}$. Thus, the angles ofθ_{inA} = 180° andθ_{inB} = 41° can be achieved. As shown in Fig. 7, the picture of the external interface of the compressed FFs was taken by an industrial digital camera. And the angles ofθ_{outA} = 138° andθ_{outB} = 108° can be measured from the picture. According to Eq.(8) and Eq.(9), we can get the volume of air V_{air} = 35.5 μL. Using Eq.(10), Eq.(11) and Eq.(12), the value of r_{out} = 12.05 mm can be obtained. Now, the two forces of F_{Mag} = 0.424 N and F_{Air} = 0.775 N can be calculated based on Eq.(7) and Eq. (13), respectively. The total force (F_{Total}) is approximately equal to 1.199 N, which is close to 1.151 N of the experimental value. More detailed information about the calculation process can be found in the supplementary material.

Fig. 8 presents the theoretical and experimental values of the static supporting force of the FFs droplet bearing. The volume of the FFs used is 600 μL. To avoid the FFs overflow, the lowest gap height is controlled at 0.6 mm. During the numerical procedure, the values of r_{out} at different gap heights can be obtained according to Eq.(10), Eq.(11) and Eq.(12). The angles of θ_{outA} and θ_{outB} are measured based on the cross-sectional image of the FFs outline. As can be seen, there's a good agreement between the theoretical data and the experimental results.

Fig. 9 shows the multicycle loading-unloading of the static supporting force of the FFs ring bearing. The volume of FFs is fixed at 150 μL. For the first cycle, as the rotor moves down, the supporting force increases. When reaching the lowest gap height of 0.25 mm, the rotor moves up and the force decreases gradually. At the height of 1.07 mm, the force of zero is detected. It indicates the pressure in the chamber is lower than atmospheric pressure due to the existence of the FFs support. Such phenomenon means that the air escape happens during the loading process. And the force became negative as the rotor elevates continuously. At the height of 1.26 mm, the negative force achieves the maximum and it turns back to zero as the rotor returns to the original height. During this stage, because of the weak sealing capacity of the FFs, the outer air goes back through the FFs ring and comes into the chamber again.

In the second loading process, the rotor shifts down at the height of 0.25 mm, and the force of 1.483 N is detected again. In this process, the air in the chamber still escapes. While for the unloading process, the rotor stopes (h = 1.07 mm) when the first zero force appears. At this

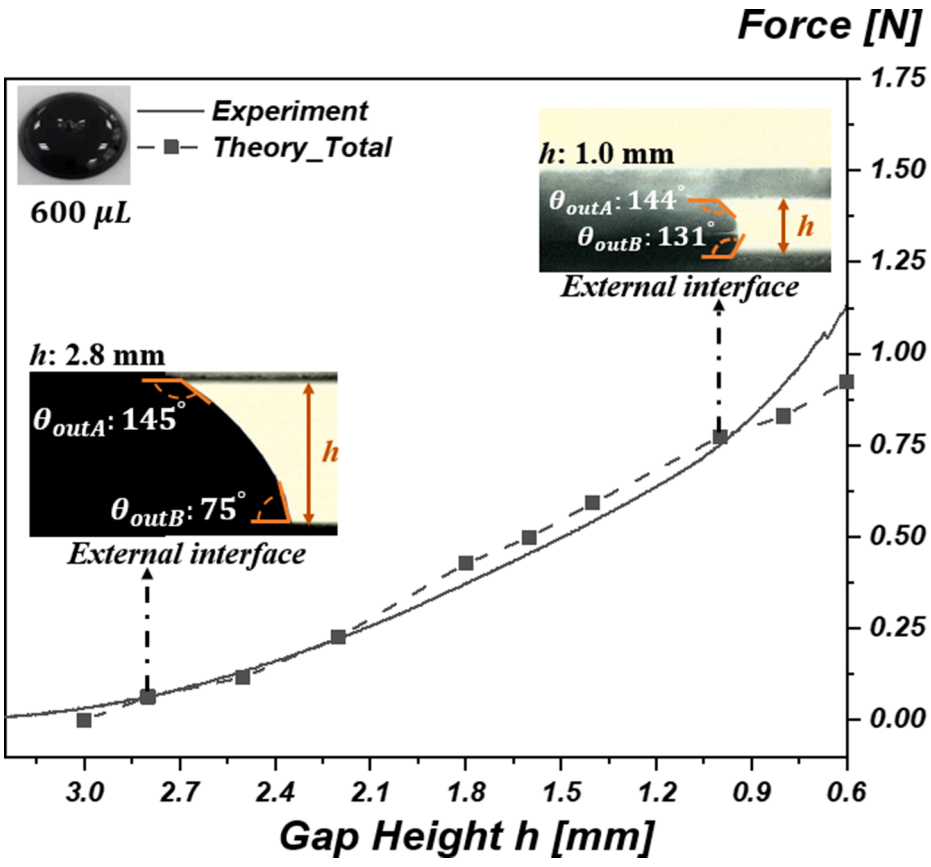

Fig. 8. Comparison of theoretical and experimental values of the static supporting force of the FFs droplet bearing.

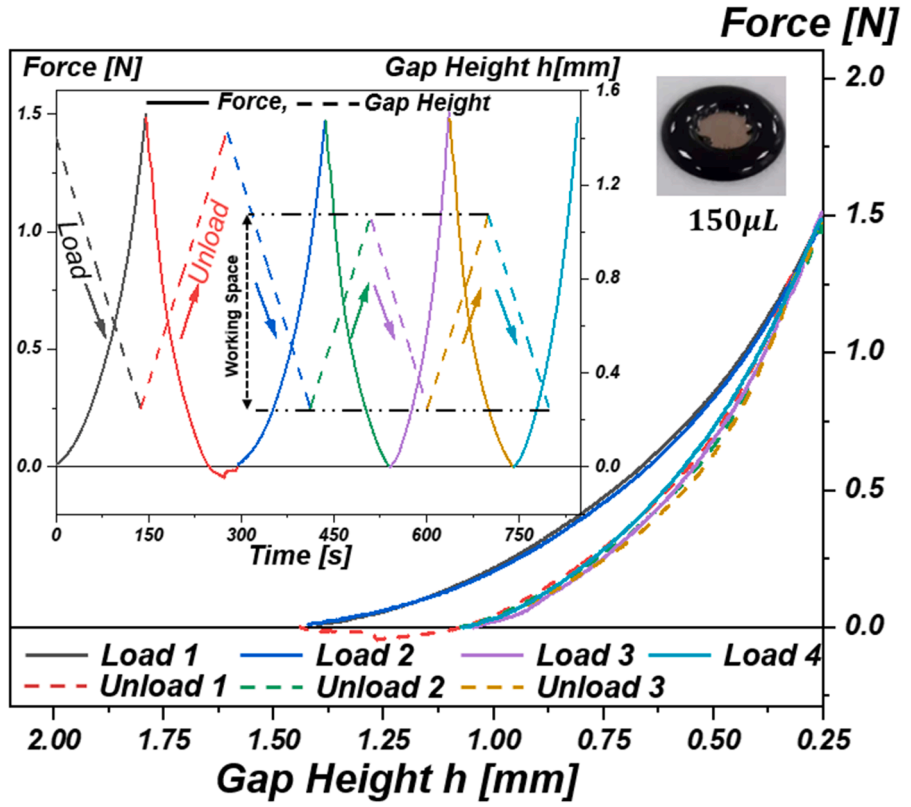

Fig. 9. Multicycle loading-unloading of the static supporting force of the FFs ring bearing.

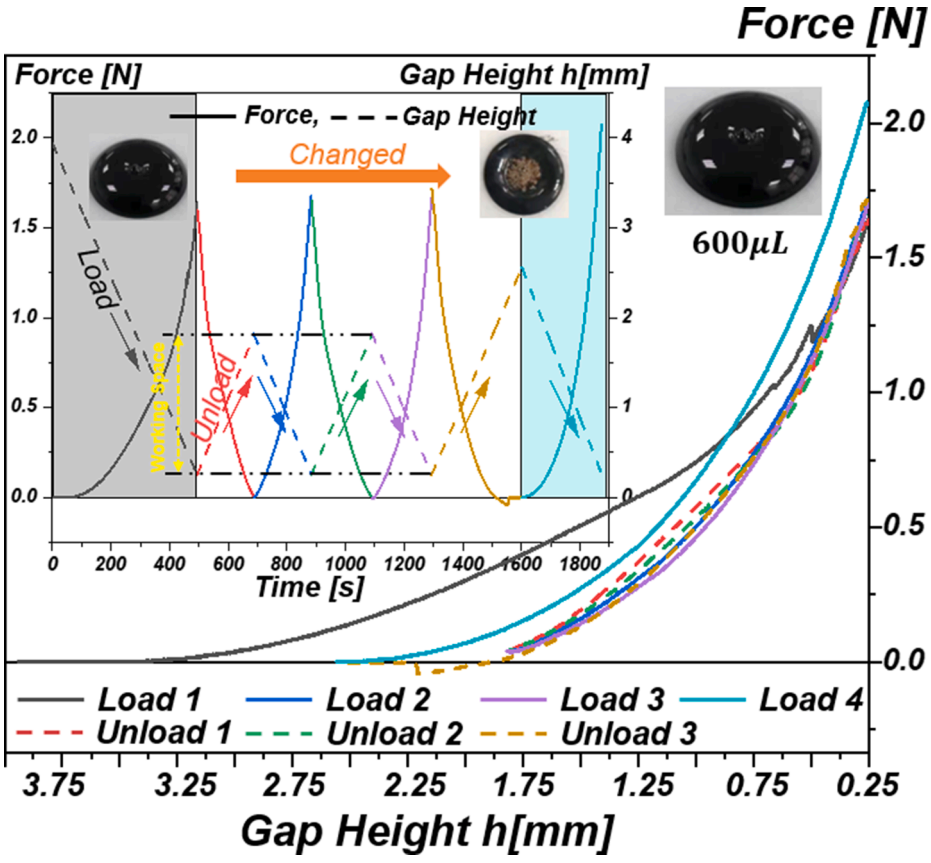

Fig. 10. Multicycle loading-unloading of the static supporting force of the FFs droplet bearing.

stage, no outer air comes back into the chamber. In the following loading-unloading process, the stroke of the rotor is controlled at the gap height of 1.07–0.25 mm. In this gap range, no air comes in/out the FFs ring and the forces of loading and unloading present a high repeatability. The height range of 1.07–0.25 mm can be defined as the working space of the ring bearing when using the FFs volume of 150 μL.

Fig. 10 shows the multicycle loading-unloading of the static supporting force of the FFs droplet bearing. For the first cycle, the rotor shifts down and force rises to the maximum value at the lowest gap height of 0.25 mm. During the loading stage, a small amount of FFs overflows the stator surface, which means the volume of the FFs maintained between the stator and rotor is lower than the original of 600 μL. In the unloading process, the rotor moves up and stops ($h = 1.84$ mm) when the force of zero is detected. In the second and the third cycles, the rotor shifts in the gap range of 1.84–0.25 mm and the forces during the loading and unloading process present good repeatability. And the gap range of 1.84–0.25 mm can be defined as its working space.

In the third unloading process, negative force appears as the height of rotor exceeds 1.84 mm. Due to the overflow of the FFs, the shape of the FFs between the gap has changed from the droplet to a new ring structure. Since the gap height increases, the sealing capacity of the FFs ring decreases. Therefore, the outer air passes through the ring and fills in the new chamber. As the rotor rise to the height of 2.46 mm, the force returns to zero again. It can be found that the bearing model changes from the original FFs droplet to FFs ring structure at this stage. In the fourth loading cycle, the maximum bearing force reaches to 2.07 N, which is a 20.7% increment compared with the previous results. The participating of the air helps to improve the total bearing capacity.

In applications, the bearings are usually working in dynamic conditions. Fig. 11 shows the dynamic supporting force of the FFs ring bearing at different rotation speeds. It can be seen that the dynamic supporting forces of the bearing are lower than that of the static force in general. Such phenomenon is more obvious at the higher rotation speed. Due to the disturbance of the centrifugation, the sealing ability of the FFs decreases, leading to the air escape from the sealed chamber. That could be the reason why the dynamic supporting forces decline. However, the dynamic supporting forces become to be more closer at the lower gap height. As pointed in Eq.(14), the total force (F_{Total}) generated by the FFs ring structure mainly relies on the magnetic field intensity in the gap. The lower of the gap height, the higher of the field intensity. Thus, the forces stabilize around 1.27 N at the gap height of 0.25 mm.

Fig. 12 presents the dynamic supporting force of the FFs droplet bearing. Different from the ring structure, the forces are close to the static supporting force at the very beginning. As the rotor moves down unceasingly, evident decline of the dynamic supporting force appears. Due to the decreased gap height, a small droplet of the FFs will overflow the surface of the stator, resulting in the fluctuation of the force curve. With the assist of the centrifugation, more FFs droplet escapes from the support interface, which leads to the decrement of the dynamic supporting force. Since the magnetic field imposes a weak restriction on the FFs at the outer interface, the rotation speeds present no obvious effect on the dynamic supporting forces.

5. Conclusions

In this paper, a simple FFs bearing structure, which consists of a rotor, a stator embedded with a cylinder magnet, and FFs is proposed. When dropping different volumes of FFs on the stator, two types of liquid structures of the ring and droplet shapes form. For the ring structure, the magnetized FFs and the air sealed in the FFs ring chamber will both supply the supporting force. While for the FFs droplet structure, only the FFs affords the liquid support. The corresponding models of the FFs bearings for the static supporting force were established and validated by experiments. The multicycle loading-unloading of the FFs

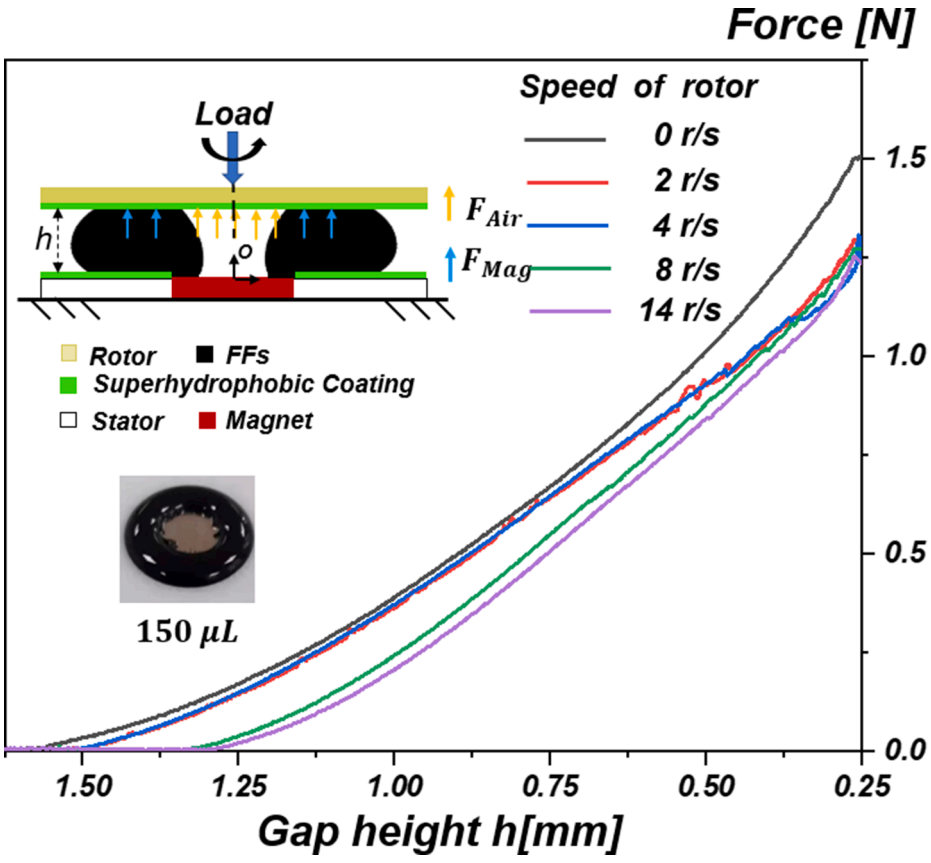

Fig. 11. The dynamic supporting force of the FFs ring bearing at different rotation speeds.

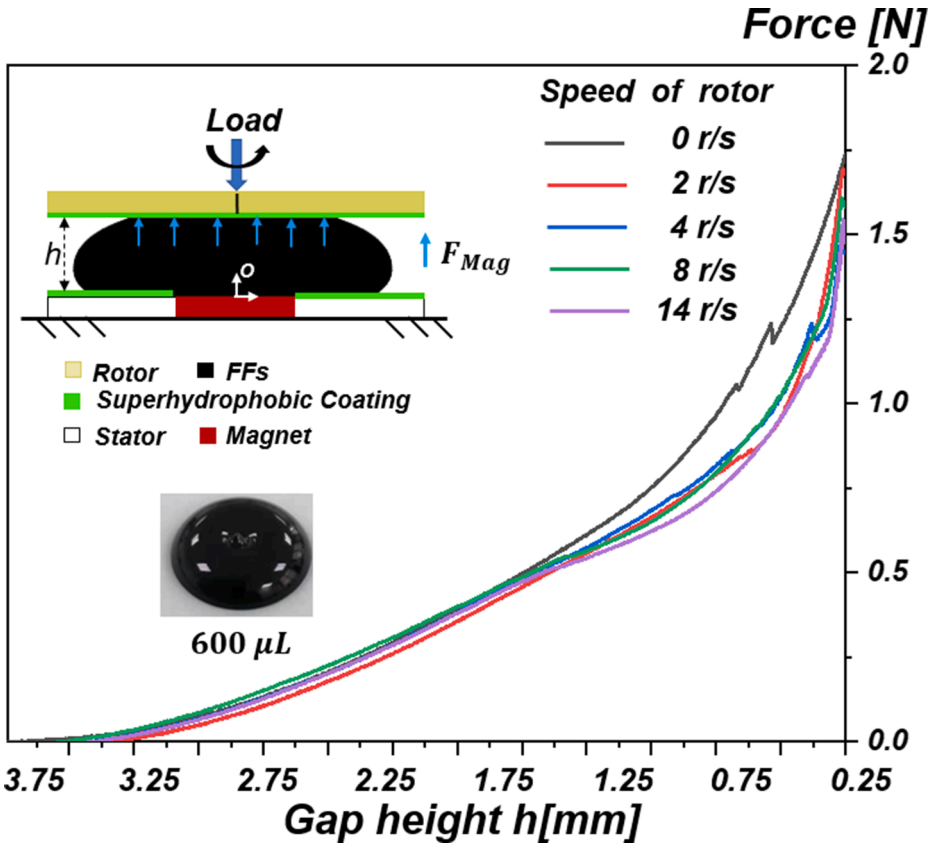

Fig. 12. The dynamic supporting force of the FFs droplet bearing at different rotation speeds.

bearings were performed. Besides, the dynamic supporting force of the bearings were also tested with different rotation speeds. The results show that the static supporting force of the bearing can be approximately predicted by the theoretical model. For the FFs ring bearing structure, the force generated by the sealed air plays a dominant role in the total force. Multicycle loading-unloading results indicate that force values with excellent repeated accuracy can be achieved only within a limited range of oscillation in gap height. Compared with the FFs droplet bearing, the rotation speed exhibits more significant impact on the dynamic supporting force of the ring structured bearing. In general, the Eq. (15) based on the model might be applied to estimate the dynamic supporting force of the bearings with low requirement. Such design presents a new way of liquid support for MEMS that requires precision supporting or frictionless bearing.

CRediT authorship contribution statement

Hao Xu: Writing – original draft. **Qingwen Dai:** Visualization, Investigation. **Wei Huang:** Conceptualization, Writing – review & editing. **Xiaolei Wang:** Supervision.

Declaration of Competing Interest

The authors declare that they have no known competing financial interests or personal relationships that could have appeared to influence the work reported in this paper.

Acknowledgment

The authors thank the National Natural Science Foundation of China (No. 51875278) for financial support.

Appendix A. Supplementary material

Supplementary data to this article can be found online at https://doi.org/10.1016/j.jmmm.2022.169212.

References

[1] P. Schiffer, Granular physics: a bridge to sandpile stability, Nat. Phys. 1 (1) (2005) 21–22.
[2] R. Maboudian, C. Carraro, Surface chemistry and tribology of MEMS, Annu. Rev. Phys. Chem. 55 (1) (2004) 35–54.
[3] M.-L. Chan, B. Yoxall, H. Park, Z. Kang, I. Izyumin, J. Chou, et al., Low friction liquid bearing MEMS micromotor, in: 2011 IEEE 24th International conference on micro electro mechanical systems (MEMS), 2011, pp. 1237–1240.
[4] M.L. Chan, B. Yoxall, H. Park, Z. Kang, I. Izyumin, J. Chou, M.M. Megens, M.C. Wu, B.E. Boser, D.A. Horsley, Design and characterization of MEMS micromotor supported on low friction liquid bearing, Sens. Actuators A: Phys. 177 (2012) 1–9.
[5] I.S.Y. Ku, T. Reddyhoff, R. Wayte, J.H. Choo, A.S. Holmes, H.A. Spikes, Lubrication of microelectromechanical devices using liquids of different viscosities, J. Tribol. 134 (2012) 012002.
[6] J. Wen, D. Dini, T. Reddyhoff, Design and optimization of a liquid ring thrust bearing, Tribol. Int. 149 (2020) 105588.
[7] J. Wen, T. Reddyhoff, S. Hu, D. Puhan, D. Dini, Exploiting air cushion effects to optimise a superhydrophobic/hydrophilic patterned liquid ring sealed air bearing, Tribol. Int. 144 (2020) 106129.
[8] G. Sun, T. Liu, P. Sen, W. Shen, C. Gudeman, C.-J. Kim, Electrostatic side-drive rotary stage on liquid-ring bearing, J. Microelectromech. Syst. 23 (1) (2014) 147–156.
[9] P.C. Fannin, Characterisation of magnetic fluids, J. Alloy. Compd. 369 (1-2) (2004) 43–51.
[10] W. Huang, C. Shen, X. Wang, Study on static supporting capacity and tribological performance of ferrofluids, Tribol. Trans. 52 (5) (2009) 717–723.
[11] S. Odenbach, Magnetic fluids - suspensions of magnetic dipoles and their magnetic control, J. Phys.: Condens. Matter 15 (15) (2003) S1497–S1508.
[12] B.L. Prajapati, Magnetic-fluid-based porous squeeze films, J. Magn. Magn. Mater. 149 (1-2) (1995) 97–100.

[13] L. Vékás, M. Rașa, D. Bica, Physical properties of magnetic fluids and nanoparticles from magnetic and magneto-rheological measurements, J. Colloid Interface Sci. 231 (2) (2000) 247–254.

[14] R.E. Rosensweig, Directions in ferrohydrodynamics (invited), J. Appl. Phys. 57 (8) (1985) 4259–4264.

[15] C. Rinaldi, A. Chaves, S. Elborai, X. He, M. Zahn, Magnetic fluid rheology and flows, Curr. Opin. Colloid Interface Sci. 10 (3-4) (2005) 141–157.